ELSEVIER

Polymer 44 (2003) 807–820

polymer

www.elsevier.com/locate/polymer

A new 'tailor-made' methodology for the mechanical behaviour analysis of rubber-like materials: I. Kinematics measurements using a digital speckle extensometry

Fazilay Laraba-Abbes[a,*], Patrick Ienny[b,1], Roland Piques[c,2]

[a]*Centre des Matériaux P.M. Fourt, Ecole des Mines de Paris, BP 87, F91003 Evry Cedex, France*
[b]*Centre des Matériaux de Grande Diffusion, Ecole des Mines d'Alès, F30390 Alès Cedex, France*
[c]*Centre des Matériaux P.M. Fourt, Ecole des Mines de Paris, BP 87, F91003 Evry Cedex, France*

Received 3 March 2002; received in revised form 1 September 2002; accepted 4 September 2002

Abstract

This paper is the first part of a work devoted to the setting-up of a methodology for the mechanical behaviour characterization of rubber-like materials, using a digital speckle extensometer. We present here the experimental approach, specific to large strain measurements. The proposed method is based on in-plane kinematics measurements using an optical extensometer. The whole two-dimensional field of in-plane displacements is obtained by a digital image processing. We discuss then the correlation calculations and how to achieve the optimal subset matching. Next, we specify how to derive the principal stretch ratios, and the accuracy on these components, issued from a subsequent numerical calibration.

Finally, we present experimental data dealing with a carbon black, filled natural rubber, issued from uniaxial traction tests, pure shear tests, and tensile tests performed on double-edge notched tensile specimens.

Keywords: Natural rubber; Large strain-kinematics measurements; Digital speckle extensometry

1. Introduction

Rubber and rubber-like materials have many industrial applications. Typical applications of these materials in mechanical systems include automotive tyres, load bearing pads, silent blocks to absorb and to control vibration, seals, springs and numerous other useful products. Modelling and predicting the behaviour of any material system requires the knowledge of the mechanical response of the material. It would be preferable to test every conceivable loading condition a material may be subjected to, and observe its performance, but this is neither practical nor possible.

Instead, standard tests are performed on a limited number of representative material samples, and constitutive models are used with the test data to predict the behaviour of the material for a wide range of loading conditions. A good analysis of the mechanical behaviour of structures needs a model which accurately represents its stress–strain response. Unfortunately, the mechanical responses of rubber, especially when subjected to complex loads, are not well understood. This is perhaps due to a combination of several reasons: (i) stress–strain behaviour of rubber is highly non-linear, (ii) the material usually experiences large strains, approximately several hundred percents, and (iii) undergoes very little volumetric changes upon deformation.

Furthermore, natural and synthetic elastomers are usually blended with fillers such as carbon black (CB) or silica. Originally, these fillers were intended to play the role of diluents, in order to cut down manufacturing costs. Very soon, however, it was realized that some of them induced unexpected properties to the processed materials. This improvement of properties like hardness, tear, tensile, fatigue and wear resistance is called reinforcement. Conversely, the inclusion of fillers to a crosslinked elastomeric matrix results in a substantial increase of hysteresis, stress-softening (Mullins' effect), permanent set and strain dependent dynamic modulus effects. Thus, the

* Corresponding author. Tel.: +333-26-50-24-75.
E-mail addresses: fazilay_abbes@hotmail.com (F. Laraba-Abbes), patrick.ienny@ema.fr (P. Ienny), roland.piques@mat.ensmp.fr (R. Piques).
[1] Tel.: +334-66-78-56-32; fax: +334-66-78-56-80.
[2] Tel.: +331-60-76-30-52; fax: +331-60-76-31-60.

0032-3861/03/$ - see front matter © 2002 Elsevier Science Ltd. All rights reserved.
PII: S0032-3861(02)00718-8

Table 1
The CB filled NR compound formulation

Formulation (phr)	
Pure gum	100.0
Zinc oxide	15.0
Stearic acid	1.0
N-772 carbon black	20.0
N-330 carbon black	3.0
Sulphur	≤2.0
Plasticizers	5.0
Accelerators	1.5
Antioxidant	1.5

determination of an accurate constitutive equation, based on a complete analysis of the mechanical behaviour of such materials, must take these phenomena into account.

In this context, the digital speckle extensometry presents several points of interest. This method gives access to a two-dimensional field of in-plane displacements, with a high spatial resolution. Furthermore, it is non-contact, non-intrusive, and it requires no preparation of the sample.

We describe here the setting-up of a methodology for the mechanical behaviour characterization of rubber-like materials, using a laser speckle extensometer. The whole two-dimensional field of in-plane displacements is obtained by a digital image processing, which is becoming increasingly important as an experimental tool. We discuss then the correlation calculations, and how to achieve the optimal subset matching. Next, we specify how to derive the principal stretch ratios, and the accuracy on these components, issued from a numerical calibration.

Using this method, a two-dimensional experimental database has been constituted, enclosing uniaxial traction (UT) and pure shear (PS) tests for the identification of the constitutive law, and tensile tests on double-edge notched specimen for its validation.

The second part of this paper [1] deals with the identification and the validation of the constitutive law, using experimental data on non-preconditioned and preconditioned natural rubber (NR), and the implementation of this constitutive equation into a finite element code. Additionally, the same methodology has been applied for the analysis of the viscohyperelastic (non-linear viscoelasticity in finite transformations) behaviour of a silica-filled silicone rubber [2].

2. The material under study

The elastomer under study is a vulcanized CB filled NR. It is obtained by calandering and is conditioned in thin rectangular sheets of 2 mm thickness. It is then very flexible. The formulation of this material is given in Table 1.

The filler concentration is approximately 23 phr (parts of CB per hundred parts of NR). Notice that two CB types are incorporated into this vulcanizate's formulation. Used in the automotive industry (silent blocks), the compound has to satisfy optimal reinforcement and dissipation requirements. Moreover, this material has to exhibit a low self-heating and a good fatigue-life-time under dynamic loadings. The characteristics of this rubber, listed in Table 2, correspond to a rubbery behaviour at room temperature. The material is also quasi-incompressible, and moderately soft.

3. The constitutive equation

The fundamental problem in the theory of elasticity is to find the correct expression for the strain energy of a body subjected to a homogeneous strain. In case of isotropy and small strains, the energy can be expressed in terms of the strains and two constants specific to the material. However, the deformation which rubber and similar substances undergo are too large to be treated within the scope of the classical theory of small strains.

There are two rather different approaches to the study of rubber elasticity. The first one is based on the statistical—also called kinetic—theory, which attempts to derive the mechanical properties from an idealized model of the microstructure of vulcanized rubber. One can mention the Gaussian network [3–5], the phantom chain [6,7], the Langevin chain [8], or the eight-chains model of Boyce and Arruda [9]. The molecular approach considers the response of the molecular network to deformation. The elasticity parameters are calculated from such quantities as finite molecular length and molecular weight between crosslinks. This approach is one of the cornerstones of the understanding of the mechanical behaviour of rubber-like materials, relative to their macromolecular nature.

The second approach treats the problem from the viewpoint of continuum mechanics. This theory builds a mathematical framework to describe rubbery response, in such a way that problems may be solved without reference to microscopic structure or molecular concepts. We have opted for such a phenomenological approach, seeking for a simple procedure for the implementation of the constitutive law into a finite element code, and its use in the analysis of rubber components.

At a fixed temperature, many elastomers are very nearly perfectly elastic for quite large quasi-static deformations from the undistorted state. In other words, hysteresis effects

Table 2
The CB filled NR characteristics

Glass transition temperature (°C)	Mean molecular weight M (g/mol)	Density	Hardness SHORE A	Poisson's ratio
~ − 70	75,000	1.12	48	0.49999

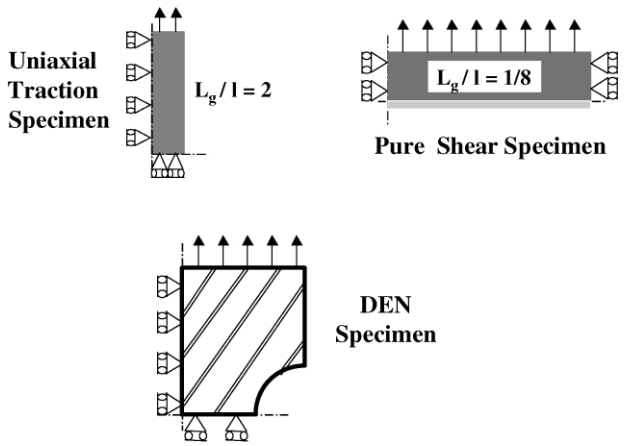

Fig. 1. Scheme of the geometry of the three tensile tests.

are neglectible. Thus, from a theoretical standpoint, it is convenient to consider these materials as perfectly elastic, and to postulate the existence of a strain density of energy function, by means of which one can characterize their mechanical behaviour. It is supposed throughout that the temperature remains constant during the loading. Furthermore, it is commonly assumed that rubber-like materials are isotropic relative to the undistorted state. They are also substantially incompressible, except under certain extreme and severe conditions (e.g. submarine conditions can induce a non-neglectible compressibility). So, both assumptions played an important role in simplifying the associated mathematical analysis.

Several strain density functions are used. On one hand, some are written in function of the dilatation tensor invariants. On the other hand, these invariants are replaced by the extension ratios. We give a brief review of the commonly used density functions in the second part of this work [1].

In our case, assuming homogeneity, isotropy (at least at the undistorted state) and incompressibility, the hyperelastic constitutive law is derived from the Rivlin's strain density function. The expansion at the third order-deformation and the retention of five parameters lead to the following expression of the strain-stored-energy function:

$$W(I_1, I_2) = c_{10}(I_1 - 3) + c_{01}(I_2 - 3) + c_{11}(I_1 - 3)(I_2 - 3) + c_{20}(I_1 - 3)^2 + c_{30}(I_1 - 3)^3 \quad (1)$$

where I_1 and I_2 are the first and the second dilatation tensor invariants, respectively, and c_{ij} the constitutive law parameters, identified from a non-linear regression procedure.

The first and the second dilatation tensor invariants are given by:

$$I_1(\lambda_1, \lambda_2) = \lambda_1^2 + \lambda_2^2 + \frac{1}{(\lambda_1\lambda_2)^2}; \qquad I_2(\lambda_1, \lambda_2) = \frac{1}{\lambda_1^2} + \frac{1}{\lambda_2^2} + (\lambda_1\lambda_2)^2 \quad (2)$$

where λ_1 and λ_2 denote the principal axial and transverse stretch ratios, respectively. Recall that a principal stretch ratio is defined as the ratio of the final length of the specimen to the initial one in the direction of the corresponding principal strain axis.

The second Piola–Kirchhoff stress tensor $\tilde{S}$, related to the undeformed state of the body, can be computed by differentiating the function W with respect to the dual right Cauchy–Green dilatation components as:

$$S_{ij} = 2\frac{\partial W}{\partial C_{ij}} \quad (3)$$

The constitutive law parameters c_{ij} are identified using a non-linear regression algorithm, typically the Levenberg–Marquardt–Fletcher [10] one. The details of the identification procedure are described in the second part of this work [1]. The experimental database includes UT and PS—also called planar tension—tests on rectangular sheets for the identification of the parameters. The principal stretches λ_1 and λ_2 are experimentally measured thanks to an optical extensometer. Furthermore, tensile tests have been performed on double-edge notched sample for the constitutive law validation. The different geometries are illustrated in Fig. 1.

4. The digital speckle extensometry

We describe here the experimental technique, that is the digital speckle extensometry. This method involves an optical laser speckle extensometer. Being non-contact and non-intrusive, optical methods are well-suited for non-destructive testing and for damage evaluation. These methods are widely used in several fields, such as solid mechanics, fluid mechanics, biomechanics and civil engineering.

The optical extensometer used here requires no preparation of the sample. It provides a two-dimensional field of in-plane displacements, with a high spatial resolution (typically 10 μm/pixel (short for picture element)). In this section, we present the extensometer's principle, the experimental setup, the digital image correlation technique, especially the principal metric functions, and finally the digital image processing, leading to the two-dimensional displacement field components.

4.1. Principle of the optical extensometer

When an optically rough object is illuminated by a coherent light such that from a laser, the surface acquires a peculiar granular appearance. This phenomenon is the result of multiple interference of light issued from different parts of the surface. The spatial variation of the intensity of light distribution is called the speckle effect. The distribution of these irregular patterns, also called objective speckles, is

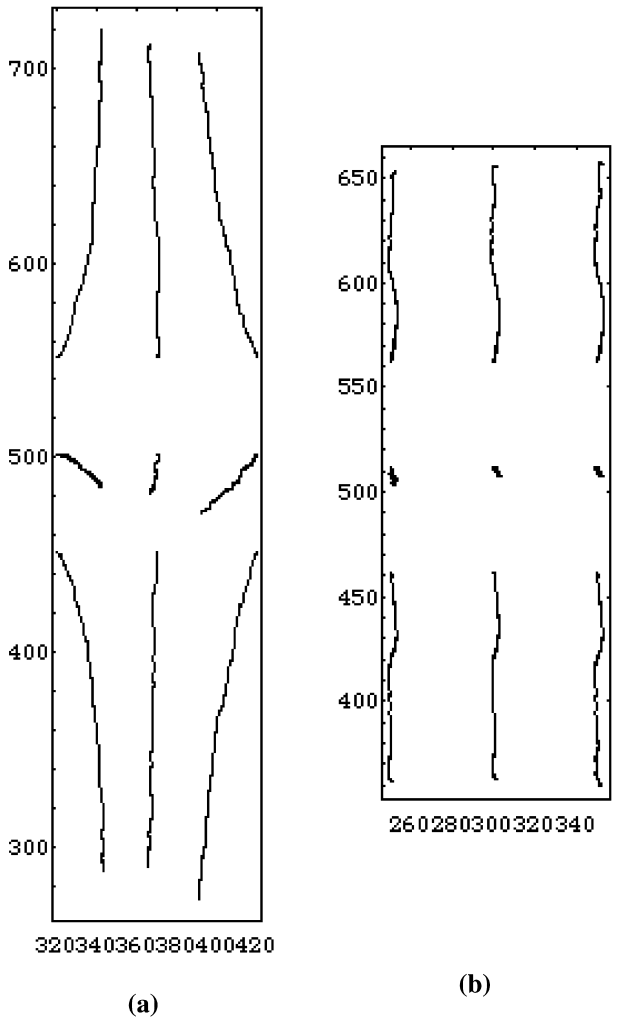

Fig. 2. Kinematics measurements (a): UT test; (b): PS test (indexes given in pixels, scale factor = 13 μm/pixel).

random, and their size is only function of the surface characteristics.

When an imaging system, say for example a charge coupled device (CCD) camera, is used, diffraction as well as interference give rise to speckle. This time, the size of the speckle patterns—called subjective speckles—depends also

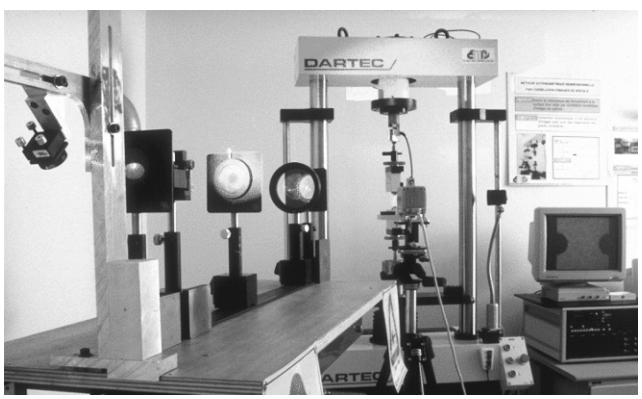

Fig. 3. The whole experimental setup.

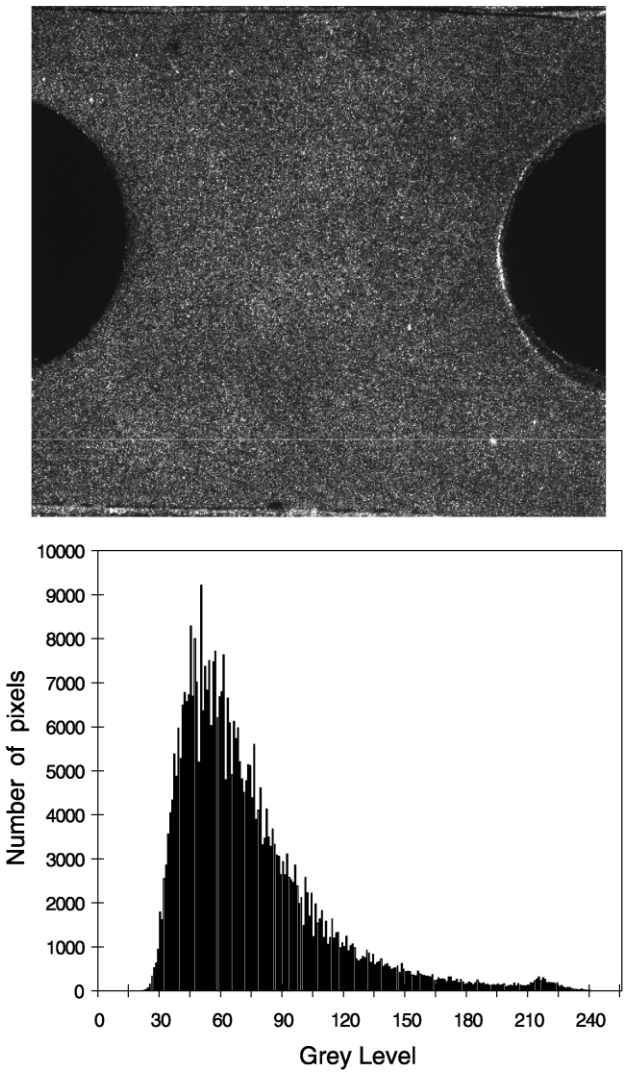

Fig. 4. A speckled DENT CB filled NR sample, and its corresponding digital grey level distribution.

on the imaging system characteristics, especially the detector aperture.

In both cases, for a given state of stress–strain of the material, these speckles are considered as optical signature patterns of the loaded object's surface. Hence, they identify the material response at a given state of the deformation. Furthermore, following these virtual markers provides the subsets kinematics, and thus the two-dimensional experimental strain field. An illustration of such a procedure is shown in Fig. 2. Nine digital markers set out on the sample allow us to keep the trajectories of the corresponding material zones in case of UT and PS tests, performed on elastomer sheets.

4.2. The experimental setup

The experimental setup is shown in Fig. 3. The test apparatus uses a 1 kN tension–compression servo-hydraulics testing machine, with pneumatic clamps. An

Argon (Ar +) laser, emitting at the wavelength $\lambda = 514.5$ nm, is the light source. An optical apparatus, comprising diaphragms and lenses, insures the expansion and the collimation of the laser beam, thus the maximum spot size and power, and the most uniform light intensity arriving on the sample. A display of a speckled sample and its corresponding histogram is illustrated in Fig. 4.

High resolution images are recorded at successive states of the deformation via a high resolution CCD camera (KODAK MEGAPLUS 1.4, (1317×1035) squared and joined pixels), set in front of the specimen. The CCD camera is fixed on a motor-driven-micro-displacement stage. This allows the camera to follow the same region under study while the lower clamps are moving. The lens axis of the camera is kept perpendicular to the surface of the sample. Its subsequent displacement during the mechanical test, synchronized to the mid-specimen point displacement, is also kept parallel to the clamps moving direction, by a previous adjustment.

The images are digitized in 1024 pixels × 1024 pixels. Each pixel represents the intensity of light arriving on the small area of the camera sensor. The value of each pixel is typically an eight-bit number (i.e. ranges from 0 to 255) with the lowest value corresponding to black, highest value to white, and intermediate values to different shades of grey. These images are stored on a PC hard disk.

4.3. The digital image correlation

A digital image is a two-dimensional signal, characterized by a light intensity distribution $\mathrm{Im}(x, y)$, function of two variables (x, y) corresponding to the in-plane two-dimensional coordinate system of the image. The determination of the two-dimensional displacement components is based on a digital image correlation. The image correlation or 'map-matching' techniques are widely used to compare two signals, in order to estimate their degree of similarity. Two fundamental methods can be mentioned. The first one, also called indirect correlation, is based on the Fourier transform, and the fast Fourier transform (FFT) if possible (in case of a 2^m digital set size). We used an alternative method, which involves direct correlation algorithms.

Consider a characteristic pattern of the image located at coordinates (x, y). Under loading, the given subset will move to a new position, located at coordinates $(x + u_x, y + u_y)$, where (u_x, u_y) are the (unknown) in-plane displacement components of the subset. The latter are deduced from a correlation calculation, by comparing subsets of numbers between two digital images.

We have to point out here that the digital subset must obviously be statistically representative of the light intensity distribution of the image. The number of pixels included in the subset, and consequently its size is thus a pertinent parameter, and is optimized following a procedure described in Section 5. In what follows, the subset is of a given size. Its spatial coordinates (x, y) are those of its geometrical centre. Furthermore, it is characterized by its grey level vector $\mathrm{Im}(x, y)$, which includes all the grey level values of the pixels constituting the digital subset.

The essential step in digital subset correlation is to find the position of 'best fit' between two similar but non-identical subsets. The match point is found by systematically displacing one subset relative to the other and computing, for each of the many possible displacements, the value of a comparison function or 'metric' that ideally, has an extremum (maximum or minimum) value at the match point. The particular displacement that produces the extremum becomes the subset displacement.

In practice, one has to achieve a correct match with the maximum of likelihood, precisely because the two subsets are not identical, owing to detector noise, real changes in the granular appearance and several other causes.

Three commonly used correlation functions [11,12], measuring the subset matching efficiency, are calculated using:

(a) the normalized inner product (NPROD) metric, defined by:

$$\mathrm{NPROD}_{\mathrm{im1,im2}} = \frac{\mathrm{Im}_1 \cdot \mathrm{Im}_2}{\|\mathrm{Im}_1\| \|\mathrm{Im}_2\|} \tag{4}$$

where Im_1 and Im_2 are the vectors corresponding to the grey level distribution of the given subset in the first and the second images, respectively, $\mathrm{Im}_1 \cdot \mathrm{Im}_2$ denotes the inner product, and $\| \|$ denotes the norm of a vector defined by:

$$\|\mathrm{Im}_1\| = \sqrt{\mathrm{Im}_1 \cdot \mathrm{Im}_1}; \qquad \|\mathrm{Im}_2\| = \sqrt{\mathrm{Im}_2 \cdot \mathrm{Im}_2} \tag{5}$$

The extremal property of this function follows from the familiar Cauchy–Schwartz inequality. Thus, $\mathrm{NPROD}_{\mathrm{im_1,im_2}} \leq 1$ for all vectors $\mathrm{Im}_1 \neq \mathrm{Im}_2$, with equality occurring only when $\mathrm{Im}_1 \equiv \mathrm{Im}_2$. This metric is widely used by several authors [13–16].

(b) the difference squared (DS) metric, defined by:

$$\mathrm{DS}_{\mathrm{im1,im2}} = \|\mathrm{Im}_1 - \mathrm{Im}_2\|^2 \tag{6}$$

Thus, $\mathrm{DS}_{\mathrm{im_1,im_2}} \geq 0$ for $\mathrm{Im}_1 \neq \mathrm{Im}_2$, with equality only when $\mathrm{Im}_1 \equiv \mathrm{Im}_2$. One can mention the work by Sutton et al. [17].

(c) the mean absolute difference (MAD) metric, given by:

$$\mathrm{MAD}_{\mathrm{im1,im2}} = \sum |\mathrm{Im}_1 - \mathrm{Im}_2| \tag{7}$$

where Im_1 and Im_2 denote the grey level distribution vectors of the subset of interest for the pair of digital images, and the sum extends over all components. As with the DS, $\mathrm{MAD}_{\mathrm{im_1,im_2}} \geq 0$ for $\mathrm{Im}_1 \neq \mathrm{Im}_2$, with equality only when $\mathrm{Im}_1 \equiv \mathrm{Im}_2$.

The work by Wessely [12] has shown that at low signal-to-noise (S/N) ratios, the NPROD algorithm leads to higher

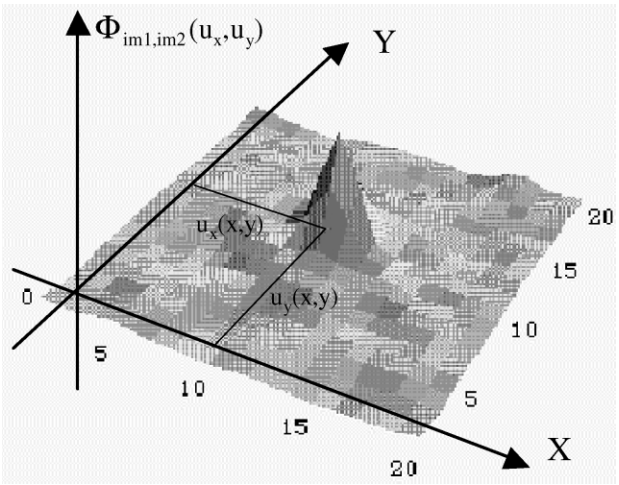

Fig. 5. Determination of the local displacement components by maximizing the correlation function.

probabilities of correct lock, but at high S/N, the MAD algorithm is preferred.

In the present work, we have used the NPROD algorithm, which is more noise resistant. In this case, our metric is given by:

$$\Phi_{\mathrm{im1,im2}}(u_x,u_y)=\frac{\sum\sum \mathrm{Im}_1(x,y)\mathrm{Im}_2(x+u_x,y+u_y)}{\sqrt{\mathrm{Im}_1^2(x,y)}\sqrt{\mathrm{Im}_2^2(x+u_x,y+u_y)}} \quad (8)$$

where $\mathrm{Im}_1(x,y)$ denotes the grey level distribution vector of the digital subset centred at coordinates (x,y) of the first image, and $\mathrm{Im}_2(x+u_x,y+u_y)$ is the grey level vector at coordinates $(x+u_x,y+u_y)$ of the second image.

The values (u_x,u_y) that maximize $\Phi_{\mathrm{im1,im2}}(u_x,u_y)$ are then the local displacement values for the given subset. The numerator of Eq. (8) is called intercorrelation function, and each member of the denominator is called self-correlation function for the corresponding image.

The subset matching efficiency is illustrated through a correlation map. The latter is defined as the correlation function values for the expected values (u_x,u_y) in a given range. Fig. 5 gives an illustration of such a correlation map.

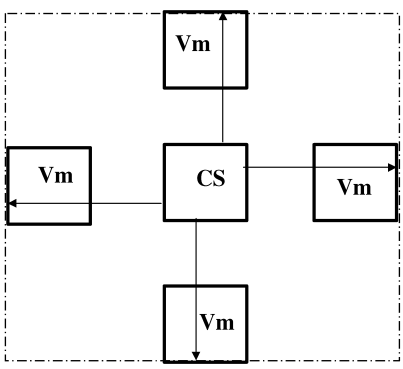

Fig. 6. The correlation parameters.

4.4. The digital image processing

We discuss here the processing of a set of digital images, recorded during a mechanical test. This procedure can be split up in two independent steps.

Recall that the CCD camera is kept in front of the sample, and its displacement is synchronized to the mid-point sample one. The CCD camera displacement value is precisely set to the half of the lower clamps displacement value. Unfortunately, a rigid body motion is superimposed to the displacement field accompanying the deformation process. We have then to extract these uniform displacement components, in order to achieve far less computation time.

The digital image processing is based on a coarse–fine search method, leading to a subpixel accuracy on the two-dimensional displacement components. We describe hereafter the digital image processing for a pair of images successively recorded during the mechanical test, this procedure being applied to the whole set of images.

The first step of the digital image processing consists in virtually meshing the reference image, that is the reference configuration. The user has to specify the number of points per each axial and transverse directions and the grid step (GS), i.e. the distance (in pixels) between two points. Each point $P(x_P,y_P)$ of the virtual grid corresponds in fact to the centre of the so-called pattern. This pattern is defined by its size, denoted 'CS' for correlation size. It is the elementary cell representative of the material particle we are tracking. Typically, nine patterns are set on the surface of the specimen. One has finally to specify the maximum displacement value V_{m} for the axial and the transverse directions. Moreover, these parameters are illustrated in Fig. 6. A first correlation calculation, performed on this predefined mesh, gives access to the rigid body displacement components. A subsequent reference change is performed on the second image, relative to the first one, in such a way that the displacement field computed at the next step is the solely deformation-process-induced one.

The second step of the pair-of-images-processing consists in evaluating the two-dimensional field of in-plane displacements. Once again, the user has to specify the correlation parameters (CS, GS and V_{m}) for a virtual mesh corresponding to a given number of digital extensometers.

A correlation computation leads to the displacement components within an accuracy of ± 1 pixel. A fine search method, based on a surfacic interpolation of the correlation function values inside the vicinity of the correlation peak (typically 3 pixels × 3 pixels), gives access to a subpixel accuracy, typically of $\frac{1}{16}$ pixel [18].

The displacement components being computed for all the material particles for the considered pair of images, we proceed to the updating of the mesh, in order to determine the two-dimensional displacement field between the next two digital images. So, the two-dimensional displacement field corresponding to the deformation process is incrementally constructed.

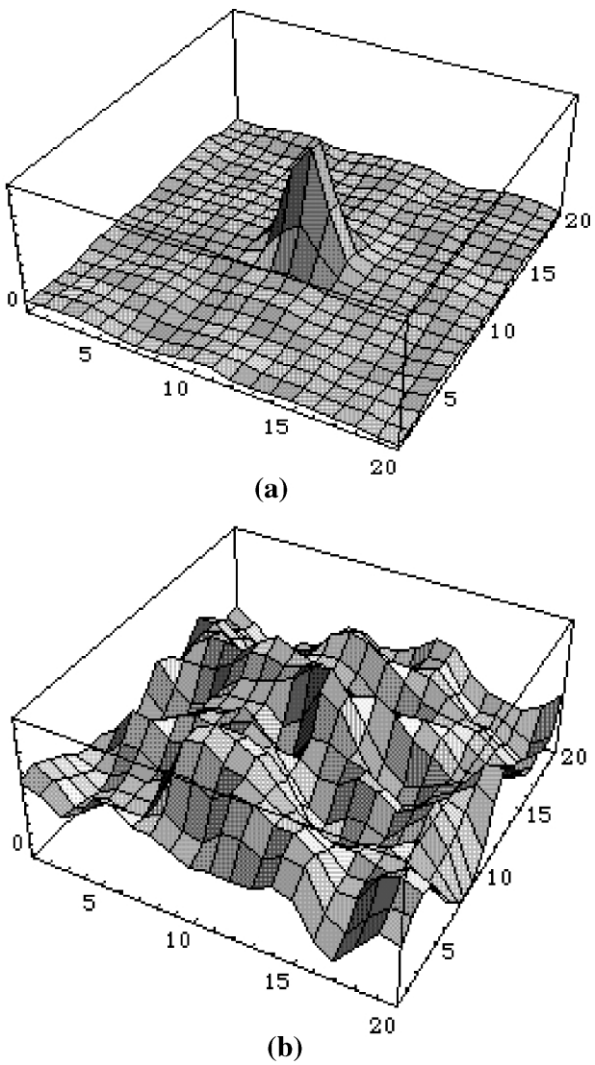

Fig. 7. Typical correlation maps for a given strain increment (a): 1 and (b): 5%.

5. Optimization of the digital image processing (experimental calibration)

This section is devoted to the optimization of the digital image processing, with emphasis on the strain increment between two images and the pattern CS. Remember that we have to achieve very large strain levels (approximately 500% of nominal strain), and to record and stock the minimum of images. To meet these requirements, we have to impose a strain increment as large as possible. In practice, we have encountered some limitations, due to speckle decorrelation. Fig. 7a and b show typical correlation maps, corresponding to a strain increment (between two images) of 1 and 5%, respectively. One maximum peak of correlation is detected in the first case, and no correlation is possible for the second one.

This illustrates then the strong dependence between the subset matching efficiency and the pattern rate of modification under deformation. As mentioned before, the digital subset size is a parameter of prime importance. We have then to relate the CS to the experimental strain increment.

5.1. The experimental calibration test

We have performed a tensile test on a rectangular sheet of CB filled NR. One hundred digital images have been recorded (data acquisition frequency of one image per 20 s), using a strain increment of 1% between two successive images. A sample of 20 digital subsets has been considered, with a CS ranging from 10 to 110 pixels. The metric function is the NPROD one. Strain increments ranging from 1 to 5% have been examined.

5.2. The calibration principle: statistical analysis of the correlation map

The experimental calibration is based on the analysis of the correlation map. The optimization of the CS related to the strain increment is achieved by considering sets of images at different steps of the mechanical test (Fig. 8). The experimental in-plane displacement components correspond to a unique correlation peak, that is the maximum of the metric function (denoted $\Delta\Phi_{\mathrm{moy}}$). We have then to detect it with the maximum of likelihood.

The enhancement of the correlation peak is achieved by a mean-elimination process [19]. We have subtracted the mean intensity of grey level of the digital subset to each pixel of the pattern, before the correlation evaluation. The elimination can be expressed as:

$$\mathrm{Im}'(x,y) = \mathrm{Im}(x,y) - \frac{1}{(\mathrm{CS})^2}\sum_{i=1}^{\mathrm{CS}}\sum_{j=1}^{\mathrm{CS}} I(x_i,y_j) \tag{9}$$

The effect of the mean-subtraction on the correlation evaluation is shown in Fig. 9. Notice that Φ refers to the metric function before the mean-elimination, and $\Delta\Phi$ denotes the metric function after it. It is seen that the correlation between the mean-eliminated images preserves much more contrast between the matching position and all the non-matching positions, because a quasi-zero-mean background is achieved in computing NPROD.

The effect of different CSs on the correlation evaluation

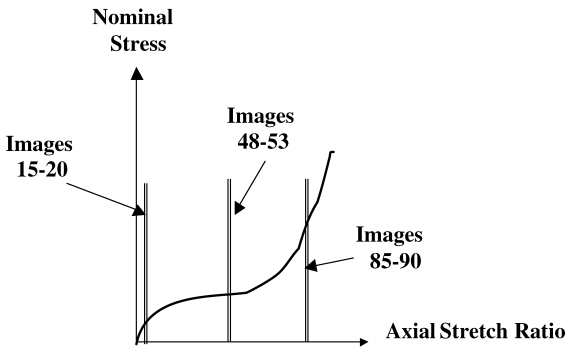

Fig. 8. The experimental calibration test.

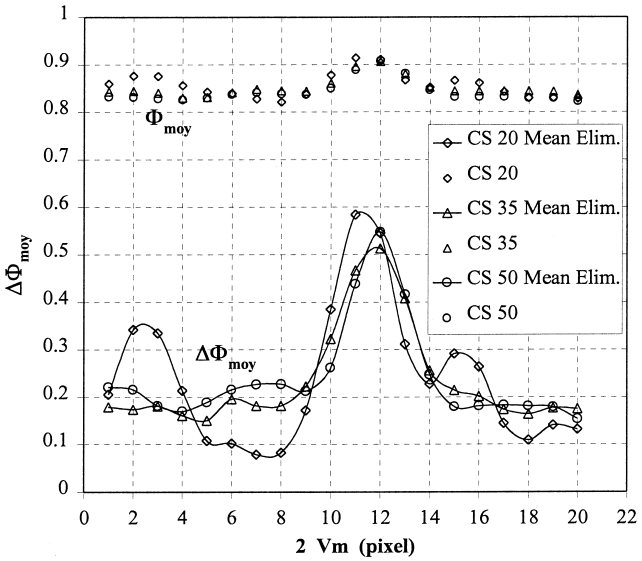

Fig. 9. The mean-elimination technique.

is also shown on the same figure. It is seen that the decrease of CS results in the flattening of the matching peak, which reduces the sensitivity or the accuracy of the measurement.

5.3. The calibration criteria

Two criteria have been used for the determination of the optimal CS:

(a) for a given strain increment and at a given step of the mechanical test, the optimal CS corresponds to solely one matching peak. In practice, the first criterion consists in counting all the peaks the height of which exceeds 90% of the maximum matching peak height.
(b) this optimal CS must be valid for all mechanical test step. In practice, three sets of digital images have been considered at the beginning, the mid and the end of the test, in order to take into account the evolution of the experimental conditions, like the sample alignment, the stabilization of the out-of-plane displacement, the surface roughness evolution during the extension and so on.

5.4. The calibration results

We have plotted the evolution of the maximum of the metric function $\Delta\Phi_{moy}$ (mean peak height value over the sample of 20 correlation maps corresponding to the 20 digital subsets used for the calibration procedure) versus the pattern CS in case of a strain increment of 3% (Fig. 10). One can note that no coherent evolution is obtained for CS ranging up to 40 pixels.

Nevertheless, we observe a stabilization of this evolution from a CS of 40 pixels. This result is corroborated by the number of matching peaks we have counted on the correlation map (Fig. 11): there is solely one peak for a

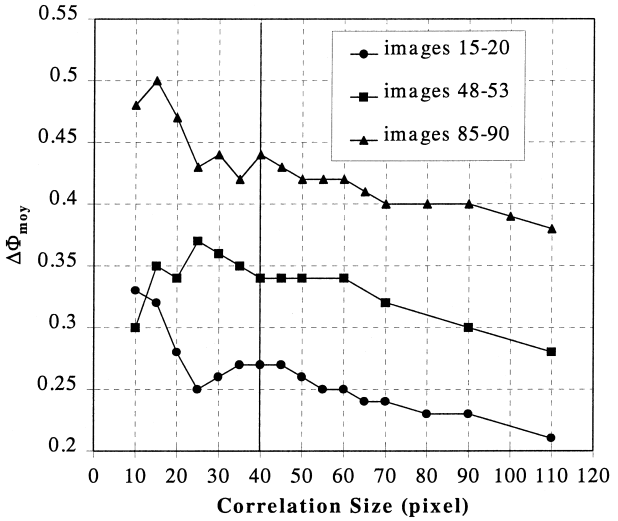

Fig. 10. Evolution of the matching peak height versus pattern correlation size (strain increment = 3%).

CS of 40 pixels. Then, for a strain increment of 3%, the optimal CS is 40 pixels.

Furthermore, one can mention the increase of the matching efficiency (Fig. 12) (increase of $\Delta\Phi_{moy}$ value) during the evolution of the test, probably due to the improvement of the sample alignment.

The same procedure has been used for strain increments of 4 and 5%. The experimental results are summarized in Table 3. Note that the optimal CS increases with the strain increment. This observation is consistent with a sufficient sampling of the signal, according to the rate of modification of the grey level distribution of the digital pattern with the strain increment.

Finally, Fig. 12 shows the decrease of the matching efficiency with the strain increment between two images, for all the mechanical test steps. Furthermore, a strain

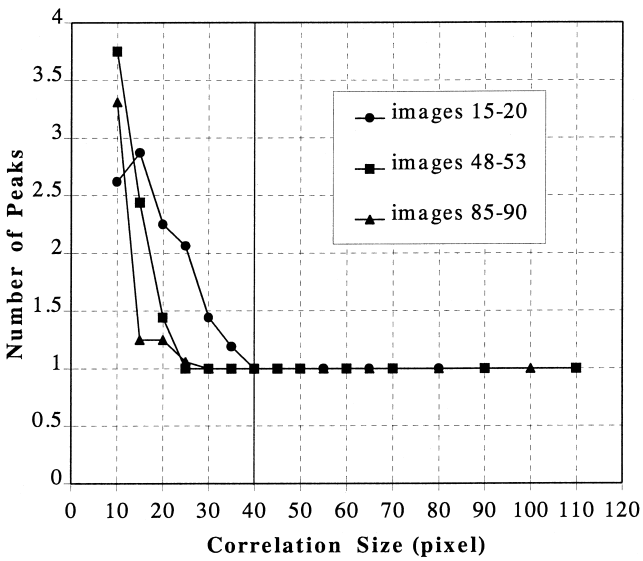

Fig. 11. Evolution of the number of correlation peaks versus pattern correlation size (strain increment = 3%).

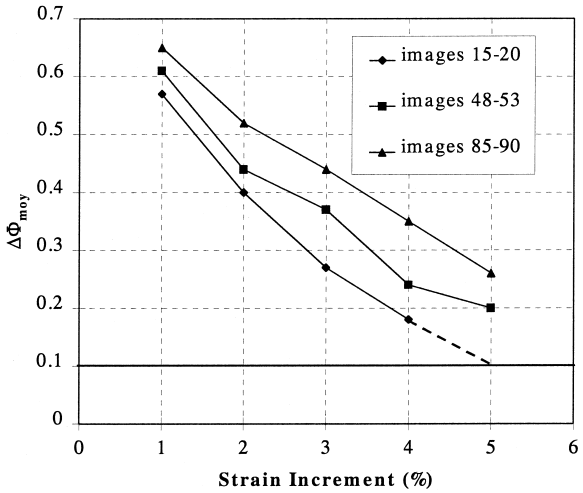

Fig. 12. Evolution of the matching efficiency with an increasing strain increment (CS = 50 pixels).

increment of 5% can induce a decorrelation at the beginning of the test. Some authors [11,19] refer to an upper limit of strain of about 6%, corresponding to a speckle mismatching.

In practice, we have imposed a strain increment about 3–4%. According to the calibration results, we have then opted for a pattern CS of 50 pixels.

6. The stretch ratios measurements

The correlation calculations give access to the kinematics of each digital pattern of the foregoing defined virtual mesh. One has then to form the gauge base, and thus the two-dimensional digital extensometer. This is performed by selecting a given number of digital patterns surrounding the subset of interest (Fig. 13). Note that we will subsequently (mis)use the term 'point' to refer to the centre of the digital pattern. Thus, the gauge's length, L_g is then function of the number of points surrounding the considered pattern, the GS between these points, and the CS of the patterns.

The determination of the principal stretch ratios is based on a local least-squares approximation of the displacement field. This is achieved by a linear fit of the displacement field gradient, provided the strain increment is small enough. Analytical expressions are then established for each component of the displacement vector. These expressions are given by:

$$u_{xcum} = a_x x + b_x y + c_x; \qquad u_{ycum} = a_y x + b_y y + c_y \quad (10)$$

Table 3
The experimental strain increment and its corresponding optimal correlation size

Strain increment (%)	CS (first criterion)	CS (second criterion)
3	40	40
4	55	55
5	/	55

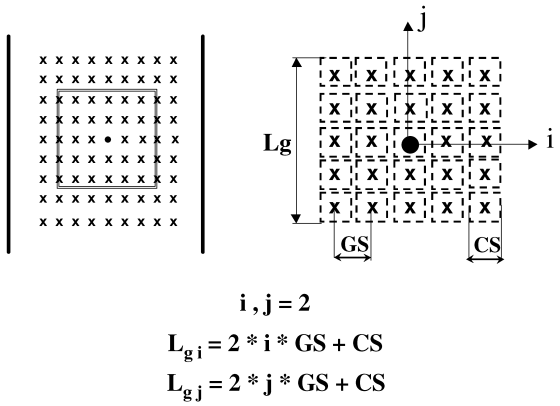

Fig. 13. Definition of the two-dimensional digital extensometer (CS: correlation size; GS: grid step).

where (a_x, b_x, c_x) and (a_y, b_y, c_y) are determined from a least-squares-fit procedure. One can then evaluate, by a spatial differentiation, the right Cauchy–Green dilatation tensor components, and thus the in-plane principal stretch ratios.

7. Numerical calibration of the principal stretch ratios measurements

Taking into account this method of spatial-differentiation-stretch-ratio-evaluation, and given the accuracy on the incremental in-plane displacement components ($\pm\frac{1}{16}\times$ pixel), a subsequent numerical calibration establishes then the accuracy on the principal stretch ratios, for tensile and PS loading conditions.

Recall that the digital image processing leads to an incremental displacement field. One has then to sum the displacement components to achieve the total extension (axial stretch ratio up to 5). The modelling of the cumulative error on the principal stretch ratios is obtained throughout two successive steps:

(a) the first one consists in evaluating the cumulative error on the summed displacement components over a given number of steps. This is achieved by generating a random summation of $\pm\frac{1}{16}$ pixel, over a given number of steps, and for each point of a virtual mesh.

The strain increment ranges from 3 to 5%, which allows us to reach a final extension of 500% of nominal strain. We evaluate then the standard deviation, and thus set the error as three times the standard deviation value. A least-squares fit of the evolution of this cumulative error versus the number of steps leads to the following expression:

$$\text{error}(n) = 0.137\sqrt{n} \quad (11)$$

where 'n' denotes the actual step. The result is illustrated in Fig. 14.

(b) the second step consists in modelling the cumulative

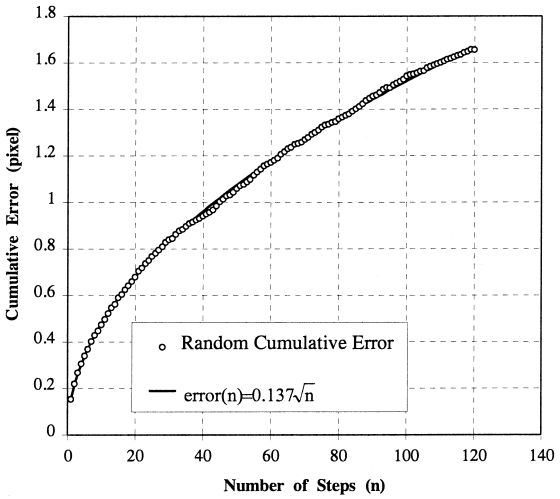

Fig. 14. Evolution of the cumulative error on the displacement components.

error on the principal stretch ratios, using the spatial-differentiation method. We have implemented a method based on a statistical perturbation of the analytical displacement fields, issued from the simulation of UT and PS tests, and taking into account the isotropy and the incompressibility of the material.

In practice, for a given step n of a mechanical test (UT or PS), the statistically perturbed-analytical-displacement components are expressed as:

$$\begin{cases} u_{x\mathrm{cum}}(n) = x_0(\lambda_2(n) - 1) \pm \mathrm{error}(n) \\ u_{y\mathrm{cum}}(n) = y_0(\lambda_1(n) - 1) \pm \mathrm{error}(n) \end{cases} \quad (12)$$

where (x_0, y_0) denote the initial coordinates of a given point of the virtual mesh with respect to the reference coordinate system, n is the actual step, and (λ_1, λ_2) are the principal axial and transverse stretch ratios, respectively.

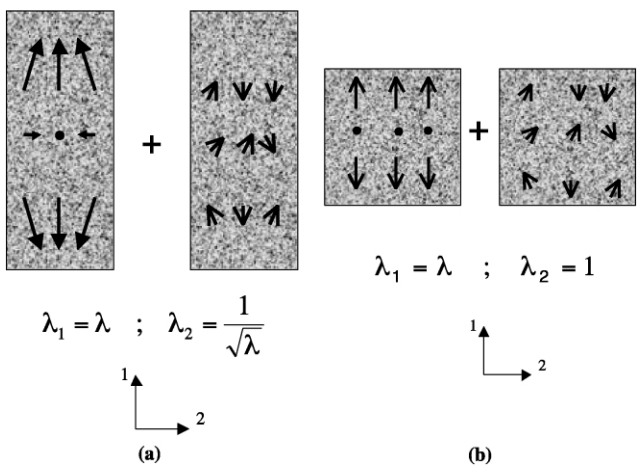

Fig. 15. Kinematics in tensile (a) and pure shear (b) loading conditions.

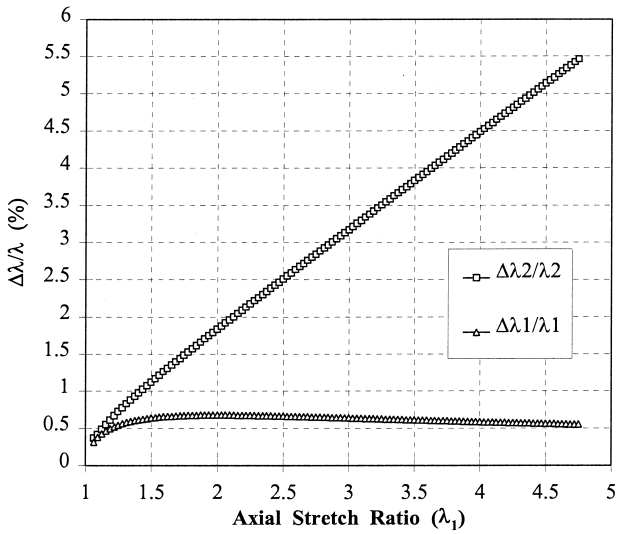

Fig. 16. Evolution of the relative error on the axial and transverse stretch ratios in tensile loading conditions (strain increment = 3%).

The boundary conditions corresponding to the mechanical tests we have simulated are illustrated in Fig. 15a and b.

The evolution of the relative error on axial and transverse stretch ratios in tensile conditions is illustrated in Fig. 16, for a strain increment of 3%. One can note the increase of the relative error on the transverse elongation, because of the decrease of the transversal gauge length. As for the axial direction, the experimental stretch ratio is determined with an increasing accuracy, the corresponding gauge length increasing this time.

The same method has been used for the simulation of a PS test. The corresponding relative errors have been computed with a strain increment of 1%. The results are illustrated in Fig. 17.

Thus, this step of the data processing allows us to validate the experimental mechanical tests. In case of UT

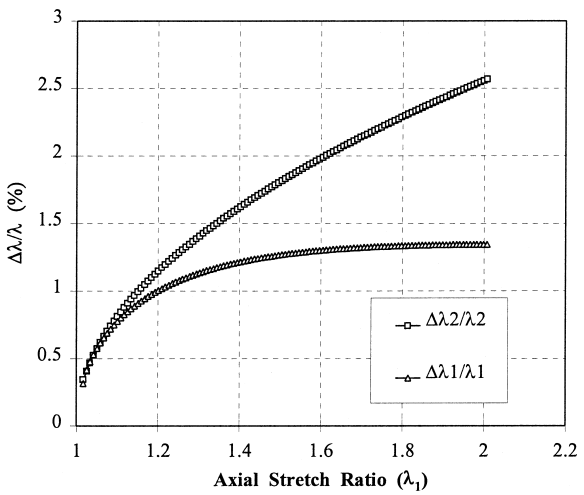

Fig. 17. Evolution of the relative error on the axial and transverse stretch ratios in pure shear loading conditions (strain increment = 1%).

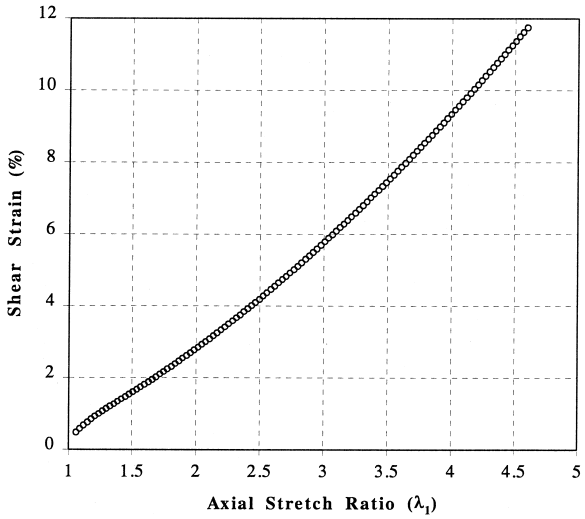

Fig. 18. Evaluation of the admissible shear strain component in uniaxial traction loading conditions (strain increment = 3%).

test, we have selected the experimental data issued from tests the shear strain component of which does not exceed 12% (Fig. 18). As for the PS test, the validation of the loading conditions relies on the so-called 'pure-shear-criterion' (Fig. 19), which allows the transverse stretch ratio to deviate from a unit value with a 2.5% accuracy.

8. The CB filled NR mechanical behaviour

The experimental results displayed here concern the mechanical behaviour of non-preconditioned CB filled NR. Effectively, as mentioned in the second part of this work, rubber-like materials generally exhibit a stress-softening effect, also called Mullins' effect. This phenomenon depends on the level of stress or strain previously seen by the material. The damage-caused-stress-softening is then increasing with this level. The identification of a unique constitutive law for the CB filled NR material, and an elastomer in general, must then take into account this phenomenon. Experimental data illustrating the stress-softening effect and its modelling are described in Part II [1].

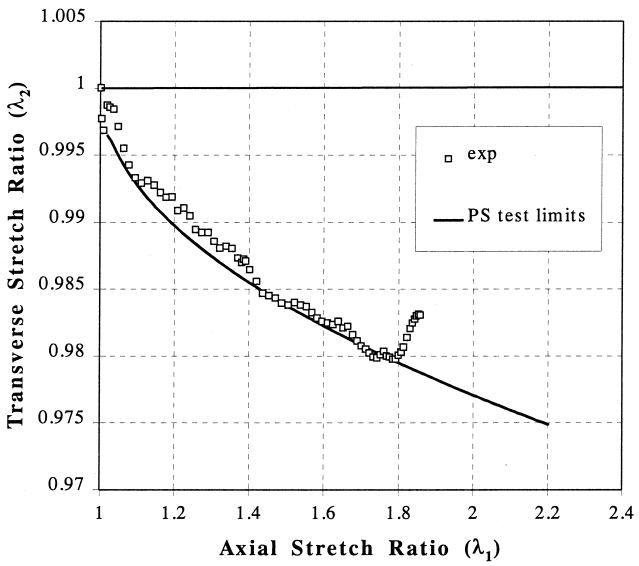

Fig. 19. Validation of a pure shear experimental data using the pure shear criterion.

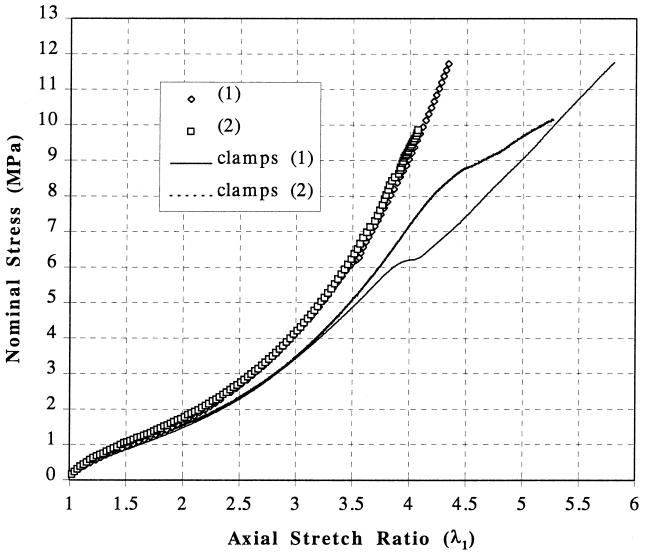

Fig. 20. Comparison between digital speckle extensometers and clamps measurements (uniaxial traction loading conditions—CB filled NR).

8.1. Uniaxial traction tests on non-preconditioned CB filled NR

UT tests have been performed on rectangular sheets of CB Filled NR. We have considered a virtual mesh of 81 points, in such a manner that nine extensometers have been set out on the sample. The tensile tests have been performed at a constant strain rate of 0.0017 s^{-1}. Both axial and transverse stretch ratios have been measured. The selection of the reliable experimental data has been performed according to the validation criteria established in Section 7.

Fig. 20 shows the mechanical responses of the non-preconditioned material in case of tensile loading conditions (the nominal stress is defined as the experimental load related to the initial section of the sample). In addition to their non-similarity, the experimental curves issued from the clamps displacements overestimate the effective extension level (up to 30% of spread). Conversely, the experimental data issued from digital speckle measurements (each plotted curve corresponds in fact to the mean measurement of the nine digital extensometers acquisition) show a good reproductibility. Furthermore, one can note the overlapping of some speckle measurement values, due to the sliding of the sample between the clamps. The digital extensometers have detected no additional extension, while the data

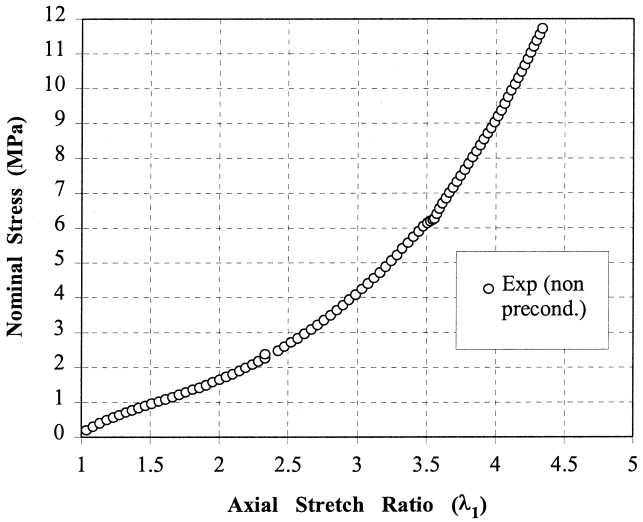

Fig. 21. Tensile response of the non-preconditioned CB filled NR (in terms of the axial stretch ratio).

corresponding to the clamps displacements shows a continuous evolution. These results illustrate then the suitability of the digital extensometry in case of large strains measurements.

Figs. 21 and 22 illustrate the evolution of the nominal stress in terms of the axial and the transverse stretch ratios, respectively. One can note the non-linear behaviour, and the stretch-induced-reinforcement of the material at high strain levels. Both the experimental axial and transverse stretch ratios have been used to determine the constitutive law parameters, using a non-linear regression algorithm we have implemented (see Part II).

Finally, thanks to the two-dimensional in-plane data measurement, one can check and validate the incompressibility hypothesis generally assumed for such material: Fig. 23 shows the evolution of the transverse stretch ratio versus the axial one. This curve is well fitted with an inverse-

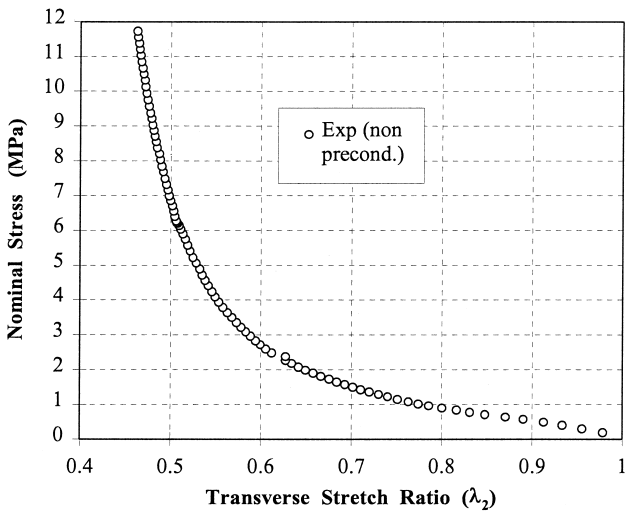

Fig. 22. Tensile response of the non-preconditioned CB filled NR (in terms of the transverse stretch ratio).

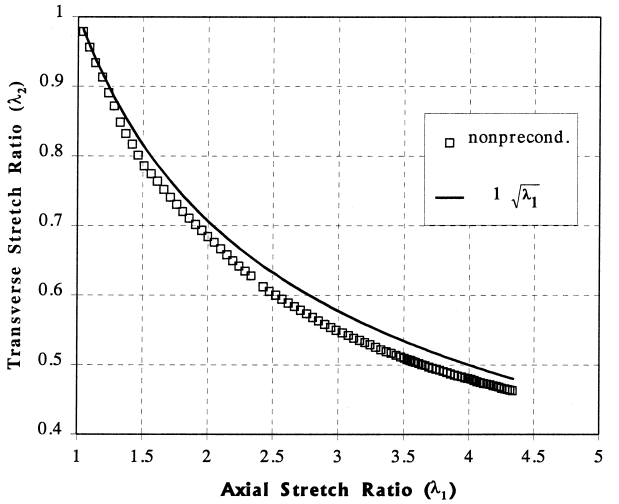

Fig. 23. Tensile response of the non-preconditioned CB filled NR: checking of the incompressibility hypothesis (assuming isotropic behaviour through the sample cross-section).

square-root function, assuming an isotropic behaviour through the cross-section of the sample.

8.2. Pure shear tests on non-preconditioned CB filled NR

PS tests have been performed on rectangular sheets cut from the same CB filled NR. As previously indicated in the case of UT tests, we considered a virtual mesh of 81 points, and thus nine extensometers. These PS tests have been performed at a constant strain rate of 0.0024 s^{-1}. Both axial and transverse stretch ratios have been measured. The selection of the reliable experimental data has also been performed according to the validation criteria established in Section 7.

Fig. 24 shows the mechanical responses of the non-preconditioned CB filled NR in case of PS loading

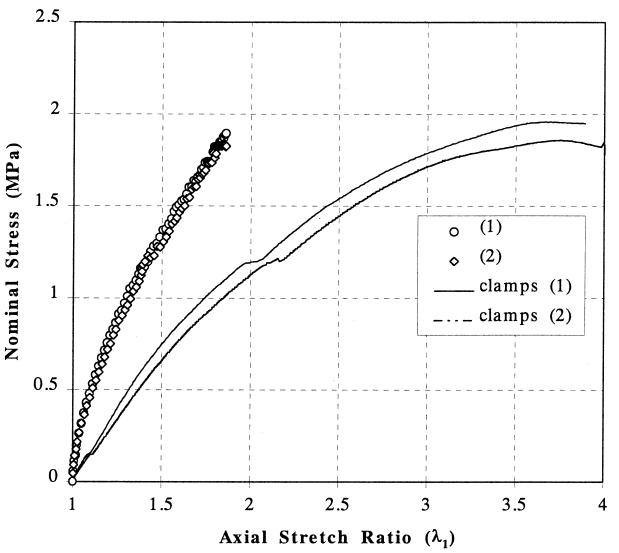

Fig. 24. Comparison between digital speckle extensometers and clamps measurements (pure shear loading conditions—CB filled NR).

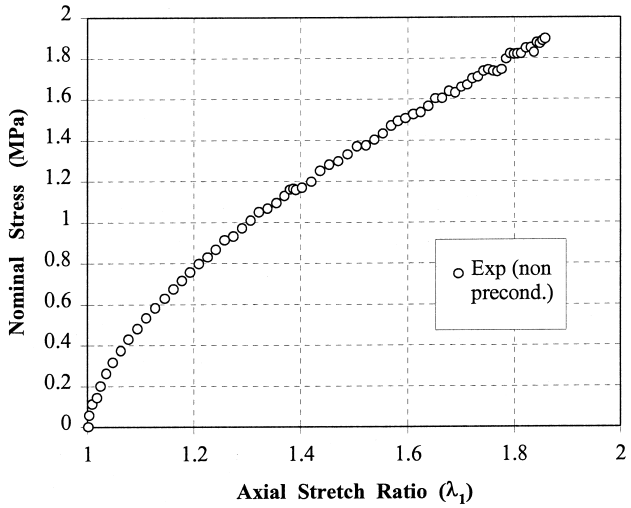

Fig. 25. Pure shear response of the non-preconditioned CB filled NR (in terms of the axial stretch ratio).

conditions. In addition to their non-similarity, the experimental curves issued from the clamps displacements overestimate the effective extension level. Conversely, the experimental data issued from digital speckle measurements show a good reproductibility.

Figs. 25 and 26 illustrate the evolution of the nominal stress in terms of the axial and the transverse stretch ratios, respectively. As for the UT results, we have used both axial and transverse stretch ratios for the identification of the constitutive equation parameters.

8.3. Tensile tests on double-edge notched tensile specimen of non-preconditioned CB filled NR

Tensile tests have been performed on double-edge notched tensile (DENT) specimen of the non-preconditioned CB filled NR. These tests have been performed using

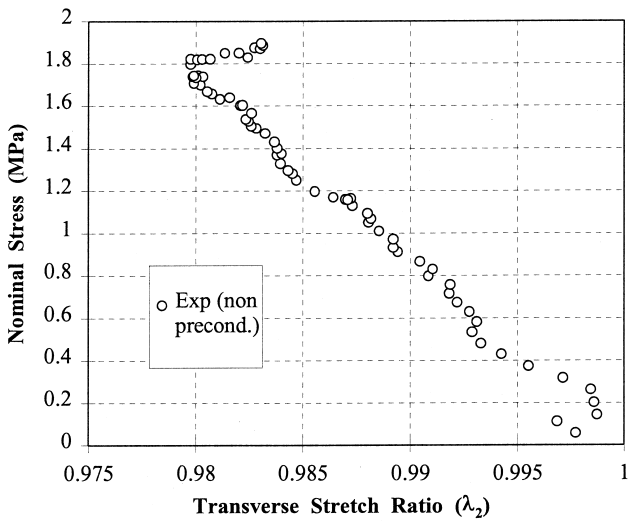

Fig. 26. Pure shear response of the non-preconditioned CB filled NR (in terms of the transverse stretch ratio).

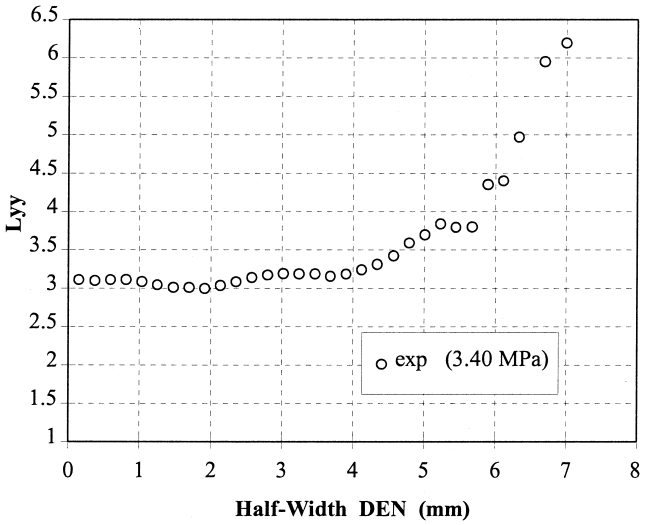

Fig. 27. Local strain measurements along the half-width of a CB filled NR double-edge notched tensile (DENT) specimen: evolution of the axial Lagrangian strain profile (L_{yy}).

a strain rate of 0.0009 s^{-1}. We have also imposed a strain increment of 1.5%, seeking for a compromise between the correlation reliability and the local-gradient-strain-measurement sensitivity, especially close to the notches. In practice, local strain measurements have been carried out by setting digital subsets between the notches. Figs. 27 and 28 show the evolution of the axial (L_{yy}) and the transverse (L_{xx}) Lagrangian strain profiles along the half-width of a DENT sample, at a given nominal stress. The pattern CS has been selected according to the calibration results of Section 5.

This application illustrates then an interesting feature of the digital extensometry, that is the local strain measurement. Furthermore, the local strain profiles have been compared to the numerical ones issued from a finite element

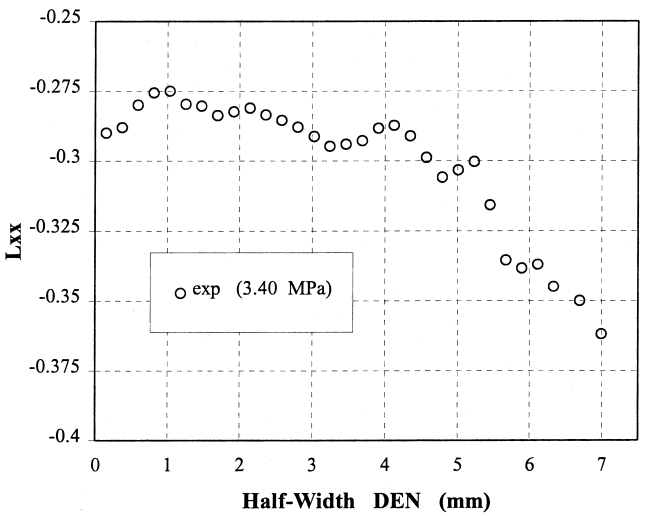

Fig. 28. Local strain measurements along the half-width of a CB filled NR double-edge notched tensile (DENT) specimen: evolution of the transverse Lagrangian strain profile (L_{xx}).

computation, for the validation of the identified constitutive law [2].

9. Conclusion and discussion

We have established a methodology for the large strain mechanical behaviour characterization of rubber-like materials, using a non-contact and non-intrusive digital speckle laser extensometry.

This experimental technique is based on digital images correlation. The correlation parameters have been optimized following an experimental calibration. The two-dimensional in-plane displacement components have been computed using a coarse–fine search method, leading to a subpixel accuracy.

The two-dimensional dilatation field has been evaluated by a spatial-differentiation-local-gradient-displacement-field approximation. We have established the accuracy on the principal stretch ratios measured in tensile and PS loading conditions, using a statistical perturbation of the analytical displacement fields. This numerical calibration allowed us to set criteria for the validation and the selection of the two-dimensional experimental data, used for the identification of the constitutive equation parameters. We have also carried out local strain measurements, for the validation of the constitutive equation.

References

[1] Laraba-Abbès F, Ienny P, Piques R. A New tailor-made methodology for the mechanical behaviour analysis of rubber-like materials: II. Application to the hyperelastic behaviour characterization of a carbon-black filled natural rubber vulcanizate, Polymer, in press.
[2] Laraba-Abbès F. PhD Thesis, Ecole Centrale de Paris, France, 1998.
[3] Wall FT. J Chem Phys 1942;10:132.
[4] Flory PJ, Rehner Jr. J. J Chem Phys 1943;11:512.
[5] Treloar LRG. Rep Progr Phys 1943;9:113.
[6] James HM, Guth E. Phys Rev 1941;59:111.
[7] James HM, Guth E. J Chem Phys 1947;15:669.
[8] Wang MC, Guth E. J Chem Phys 1952;20:1144.
[9] Arruda EM, Boyce MC. J Mech Phys Solids 1993;41(2):389.
[10] Fletcher R. Practical methods of optimization. New York: Wiley; 1987.
[11] Bailey HH, Blackwell FW, Lowery CL, Ratkovic JA. United States Air Force Project Rand Report, 1976; R-2057/1-PR.
[12] Wessely HW, United States Air Force Project Rand Report, 1976; R-2057/2-PR.
[13] Peters WH, Ranson WF, Sutton MA, Chu TC, Anderson J. Opt Engng 1983;22(6):738.
[14] Chu TC, Ranson WF, Sutton MA, Peters WH. Exp Mech 1985;25(3): 232.
[15] Bruck HA, McNeill SR, Sutton MA, Peters WH. Exp Mech 1989;261.
[16] Sutton MA, Cheng M, Peters WH, Chao YJ, McNeill SR. Image Vision Comput 1986;4(3):143.
[17] Sutton MA, Wolters WJ, Peters WH, Ranson WF, McNeill SR. Image Vision Comput 1983;1(3):133.
[18] Ienny P, Forner A. IMQ Conference, Toulon, France, 1995.
[19] Chen DJ, Chiang FP. Exp Mech 1992;145.